

3D Image Deblur using Point Spread Function Modelling for Optical Projection Tomography

Xiaoqin Tang¹, Gerda E. M. Lamers² and Fons J. Verbeek^{1,2}

¹Leiden Institute of Advanced Computer Science, Leiden University, Niels Bohrweg 1, Leiden, Netherlands

²Institute of Biology Leiden, Leiden University, Sylviusweg 72, Leiden, Netherlands

Keywords: 3D Imaging, Point Spread Function, Optical Projection Tomography, Magnification, Deblur.

Abstract: Optical projection tomography (OPT) is widely used to produce 3D image for specimens of size between 1mm and 10mm. However, to image large specimens a large depth of field is needed, which normally results in blur in imaging process, i.e. compromises the image quality or resolution. Yet, it is important to obtain the best possible quality of 3D image from OPT, thus deblurring the image is of significance. In this paper we first model the point spread function along optical axis which varies at different depths in OPT imaging system. The magnification is taken into account in the point spread function modelling. Afterward, deconvolution in the coronal plane based on the modelled point spread function is implemented for the image deblur. Experiments with the proposed approach based on 25 3D images including 4 categories of samples, indicate the effectiveness of quality improvement assessed by image blur measures in both spatial and frequency domain.

1 INTRODUCTION

1.1 Background: 3D Image Deconvolution

In biomedical research, i.e. disease and drug research, optical techniques allow efficient and high-resolution imaging of animal cell, tissues, organs and organisms. Compared to 2D imaging, 3D imaging provides more structural and comprehensive information, producing more reliable and convincing evidence for research.

Optical projection tomography (Sharpe et al., 2002), is a typical optical 3D imaging technique for objects at tissue-, organ- and organism-level in the magnitude range of millimeters, thereby filling a gap between confocal and computational tomography imaging in the resolution range. A point object located within the DOF of the optical system is considered to be in focus, but not necessarily at an optimal focus. Beyond the DOF, the object is out of focus (Walls et al., 2007). Depth of field (DOF) is defined as a double fan symmetric around the focal plane. For OPT imaging and reconstruction, the DOF is expected to be large enough to contain as much of the sample as possible. In this manner the parts of the sample located in the DOF will result in an image

more or less in focus. However, according to previous studies (Walls et al., 2007, McNally et al., 1999), large DOF subsequently produces image blur and results in low in-focus image quality. In this paper the image quality is also referred to as image resolution according to some literatures. The trade-off between DOF and image quality should be considered when selecting lens for an OPT imaging system. A lens with small numerical aperture (NA) will produce large DOF, allowing imaging of larger samples but it results in a relatively blurred image.

One typical way to improve the image quality to the best resolution is applying deconvolution to the raw tomography 2D images by using a constant theoretical or experimental point spread function (PSF). However, this approach is not strictly suitable for OPT images; the raw OPT images normally integrate the sample information of different depths within a wide field. The imaging PSF within the field varies at different depths along the optical axis. Considering this variation of the PSF makes deconvolution of 3D image more feasible and promising. A 3D image is reconstructed from the OPT images which are obtained by rotating the specimen and acquiring a series of wide-field images at regular angular intervals. This is accomplished over a full revolution of the specimen. The filtered

back-projection (FBP) algorithm is typically used for 3D image reconstruction (Kak et al., 2001) in this case. Deconvolution implemented on the reconstructed 3D image is regarded as 3D image deconvolution.

According to Chen et al., (2012), OPT is typically undertaken with specimens that extend beyond the confocal parameter i.e. the Rayleigh range, of the imaging lens. Therefore, the tangential resolution of the reconstructed 3D image decreases away from the focal plane radially. When the focal plane is coincident with the center of rotation (COR), the tangential resolution decreases centered on the COR in a radial-symmetrical fashion. For an imaging system with a focal plane located away from the COR the decrease in resolution is more complicated but the highest resolution is still found around the focal plane. The focal plane in the reconstructed slice corresponds to a circle centered around the COR, rather than a point coincident with the COR. This subsequently appears as a cylindrical surface in the 3D image centered by the COR.

The aim of our contribution lies in deblurring the OPT 3D image (improving the visual resolution) by means of deconvolution, based on the modeled PSF of the imaging system. This will, for large samples with focal plane being at or away from the COR, recuperate the imperfections of 3D image resulting from the imaging system. The method in the modelling of PSF will be explained in Section 2 and the qualitative and quantitative image comparison will be presented in Section 3. In section 4 we will present our conclusions.

1.2 Related Works

Accounting for the trade-off between large DOF and high resolution, previous studies have proposed several methods to solve the problem. One approach is choosing a high NA lens to acquire a high-resolution image and combining multiple focal planes in a simultaneous manner (Chen et al., 2013) or scanning the focal plane through the sample (Miao et al., 2010). These multiple focal plane approaches solve the issue of narrow DOF, but the mechanism of multiple measurements and scanning increases the acquisition time and the complexity of the imaging system. Considerably another direction is to use a reasonable NA lens and deblur the image by employing a deconvolution or filter on images before or after reconstruction. Walls et al., (2007) first applied the frequency-distance relationship (FDR) (Xia et al., 1995) to OPT. The corresponding filter was implemented on the sinogram before

reconstruction. The quality of the 3D image can be further improved with weighted filtered back projection (WFBP) (Darrell et al., 2008); this is done by considering the intensity distribution of multiple fluorescent spheres of known size along the optical axis. But the implementation of evenly placing each sphere along the optical axis is rather difficult to achieve. Chen et al., (2012) proposed a way to determine the modulation transfer function (MTF) that contributed to MTF-mask filter and MTF-deconvolution filter in the reconstruction process. The former filter significantly reduced the artifacts produced by sparse projection but the latter filter had limited improvement on tangential image resolution. Additionally, a spatial-invariant experimental PSF was investigated by McErlean et al., (2016) in order to improve the spatial resolution. However, spatial-invariance of the PSF is not completely convincing for OPT. Most recently, a new deconvolution approach based on the reconstructed 3D image was proposed by Horst et al., (2016). In their approaches the PSF was modelled and as such they achieved significant improvement on the reconstructed slice. Nevertheless, they focused on the deconvolution of vertically independent slices and omitted the PSF diffractions along the optical axis that concerns the interaction of different slices.

In this paper, we contribute by modeling the experimental PSF of a single sphere along optical axis, thereby considering the interaction of contiguous slices from the reconstructed volume. At the same time, the magnification is taken into account in an experimental manner. As discussed in section 1.1, the tangential resolution of the OPT 3D image slice decreases radially around the focal plane. Theoretically the best resolution of the reconstructed 3D image can be achieved by combining all the coronal deconvolutions of different angles. The coronal deconvolution means deconvolving the 3D image with the PSF slice by slice in the coronal plane along its depth axis. This depth axis is parallel to optical axis of the modelled PSF. We only implement the coronal deconvolution in 2 opposite angles, i.e. the reconstructed 3D image and its opposite sample at 180° centered by the COR, in parallel considering the enormous time consumption of 3D matrix rotation in N angles and the symmetry of the focal plane. When the focal plane is off the COR during imaging process, the shift is accounted for by a shift in PSF modelling. This paper focuses on the presentation of the concept of PSF modeling and coronal deconvolution on 3D OPT data, accompanied by some initial experimental results based on 25 3D images including 4 categories of samples. Further

evaluations on a larger number of data are the topics of our current research.

2 MATERIALS AND METHOD

2.1 The OPT Imaging System

Our homemade OPT imaging system consists of a Leica MZ16 FA stereomicroscope with a Plan 0.5 \times and 135mm working distance objective lens (Leica 10446157). Images are acquired by a 1360 \times 1036 pixel Retiga Exi CCD with a well size of 6.45 $\mu\text{m}\times$ 6.45 μm and saved as 12-bit tiff-files. A full revolution results in a 1.13Gb tiff-file. The acquisition is accomplished by a rotation of the specimen driven by a stepper unit; the stepper moves 0.9 $^\circ$ per step and it results in 400 images per revolution. The OPT imaging system has two modules: for bright-field imaging the specimen is illuminated with a LED and for fluorescence imaging a 100W mercury lamp is used in combination with a filter-block (GFP1, Texas Red).

2.2 Sample Preparation of a Single Fluorescence Sphere

To image the specimens in the range of several millimeters small-valued NA (effective NA: 0.0105~0.0705) lens is used to obtain the large DOF in our OPT imaging system. The resolution of an optical system is defined as the minimum distance r at which two separate points can be distinguished as individuals. According to the Rayleigh criterion $r = 0.61 * \lambda/NA$ for a circular aperture where $\lambda = 509 \text{ nm}$ is the emission wavelength, the minimum size of the experimental fluorescence sphere is supposed to be in the range between 4.40 μm and 29.57 μm . To make it visible in the image the sphere size is supposed to exceed this range. In our case, we choose the green fluorescent protein (GFP) sphere of size 43.2 μm and diluted it to a concentration of 360 beads/ml.

To image and model the PSF along optical axis we have developed an injection-based protocol to place the spheres into agarose as follows:

- 1% low melting point (LMP) agarose, cool down to \sim 37 $^\circ$;
- Drill cylindrical agarose shapes when it is semi-solidified in a petri dish;
- Inject the diluted spheres into the outer wall of the agarose along a line parallel to the central axis, preferably with a small size syringe. In our case a

0.5 ml syringe is used with a needle length of 13mm and diameter of 0.29mm, as shown in Figure 1;



Figure 1: The injection protocol with green spots indicating the injection position where fluorescence spheres may occur. The cylinder corresponds to the shape of the agarose.

- Keep the agarose at 4 $^\circ\text{C}$ until it is fully solidified (\sim 3 hours);
- Clear the sample with 70%, 80%, 90%, 96%, 100% ethanol, 100% ethanol: BABB (benzyl alcohol: benzyl benzoate = 2: 1) = 1: 1 and BABA.

Our goal is to acquire the images of a single sphere placed at different depths along optical axis. Therefore, randomly sprinkling the spheres into the agarose in a traditional way is not feasible. The main reason is that there may be interactions and overlap between different spheres either at the same or different depths. This makes the extraction of the single sphere image difficult or even impossible. The images of each single sphere at different depths are acquired by means of sample rotation. Each rotation corresponds to a different depth in the OPT imaging system. The straight-like sphere injection method in of our protocol significantly reduces the probability of overlapping between different spheres. In this way the images of the same sphere in a full revolution can be easily and efficiently acquired. The OPT imaging system and environment is configured as explained in (Tang et al., 2017).

2.3 PSF Modelling Concerning Different Magnification

For our experiments a full revolution of 400 images of the single GFP sphere are acquired. In Figure 2 the processes of sphere image acquisition and PSF modelling are presented. In Figure 2(a) and (b), the green dot represents the sphere and the red arrow indicates the sphere rotation. The excitation and emission beams are regarded to be parallel, demonstrated as blue and green beams in Figure 2(a). For PSF modelling, the focal plane is set at the COR. The 3D image whose focal plane is shifted from the COR, requires an equal shift in the PSF. With the protocol (cf. section 2.2) the physical rotation radius of the sphere r_b can be easily measured. To this end, we first measure the radius of the cylindrical agarose r_c and image it in the bright-field mode with small

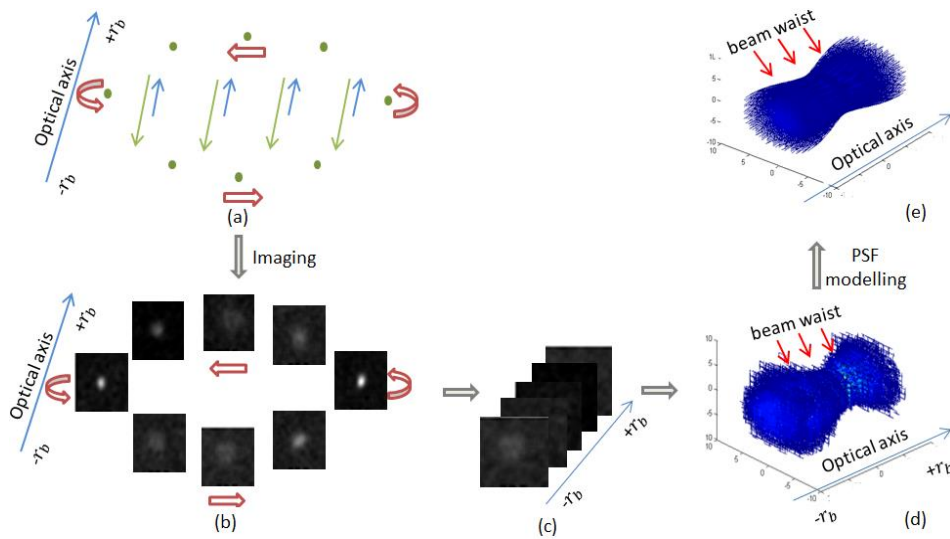


Figure 2: Image acquisition and PSF modelling of a single GFP sphere. (a) The light path of the OPT imaging system that passes through GFP spheres (green dots). The excitation beams and emission beams are separately shown in blue and green arrows. (b) Images of the single sphere acquired at different angles. (c) Images of the single sphere stacked according to the defocus. Half rotation with defocus from $-r_b$ to $+r_b$ is required, in our experiment $r_b = 3\text{mm}$ as calculated from Eq. (1). (d) The experimental and discrete PSF with defocus from $-r_b$ to $+r_b$. (e) The modelled and continuous PSF with defocus from $-r_b$ to $+r_b$.

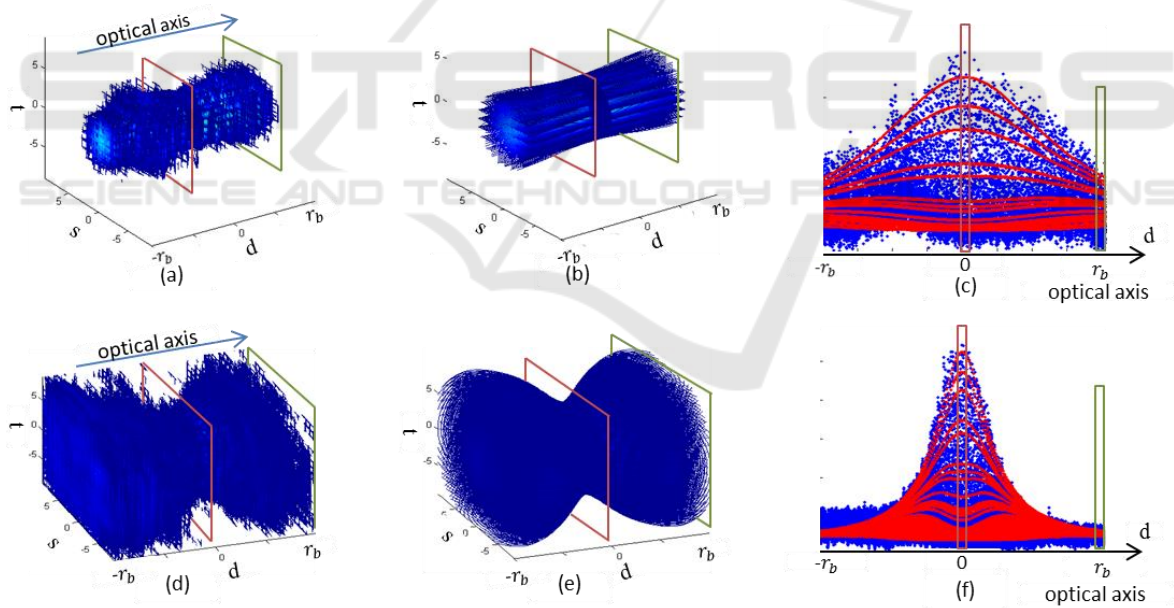


Figure 3: PSF modelling along the optical axis. (a), (d) Experimental PSFs acquired from images at magnification of $12.5 \times$ and $25.0 \times$. (b), (e) The corresponding modelled PSFs using Eq. (4) and Eq. (5). All the voxels of experimental data in (a) and modelled data in (b) are respectively transformed to blue and red dots in 1D functional in (c) to visualize the modeling performance. The vertical axis in (c) displays the intensity that corresponds to the voxel intensity in (a) and (b). Similarly, voxels in (d) and (e) are transformed to the data in (f).

exposure time. In the same experimental environment, the sphere is afterwards imaged in the fluorescence mode. r_b is calculated by Eq. (1).

$$r_b = \frac{d_{bi}}{d_{ci}} \cdot r_c \quad (1)$$

with d_{bi} representing the rotation diameter of the sphere in the tomogram, achieved by measuring the distance of two opposite sphere centers that are both in focal plane. d_{ci} is the diameter of the cylindrical agarose in the bright-field image. Dividing r_b by 100 rotations, the distance of each rotation along optical axis is determined. In our case the measured $r_c = 4\text{mm}$, $d_{bi}/d_{ci} = 0.751$, producing $r_b \approx 3\text{mm}$. Therefore, the physical distance of two adjacent rotations along optical axis is approximately $30\mu\text{m}$.

According to convention the imaging PSF is assumed as a focused Gaussian-like beam:

$$p(s, t, d) = \frac{1}{2\pi\sigma(d)^2} \cdot \exp\left(-\frac{s^2 + t^2}{2\sigma(d)^2}\right) \quad (2)$$

where $\sigma(d)$ is the beam waist (Figure 2) given by:

$$\sigma(d) = \sqrt{\sigma_0^2 + \left(\frac{\lambda d}{\pi\sigma_0}\right)^2} \quad (3)$$

With σ_0 the Gaussian beam waist defined as the $1/e$ value of the field amplitude in focus (van der Horst *et al.*, 2016), λ the emission wave length of fluorescence spheres and d the defocus along optical axis. For a specific magnification, σ_0 is constant, but it varies when imaging with different magnifications. Additionally, in Eq. (2) and Eq. (3) the beam waist $\sigma(d)$ is typically regarded as the standard deviation of the Gaussian model in previous studies (van der Horst *et al.*, 2016). Different from the Gaussian model in (van der Horst *et al.*, 2016), we generalize the model by employing parameter ρ_1 , ρ_2 and ρ_3 as:

$$p(s, t, d) = \rho_1 \cdot \frac{1}{2\pi\sigma(d)^2} \cdot \exp\left(-\frac{s^2 + t^2}{2\sigma(d)^2}\right)^{\rho_2} + \rho_3 \quad (4)$$

Instead of equalizing the beam waist and standard deviation as described in (van der Horst *et al.*, 2016) and (Kogelnik *et al.*, 1966), we investigate the relationship between them by multiplying a parameter a with beam waist, considering different magnifications.

$$\sigma(d) = a \cdot \sqrt{\sigma_0^2 + \left(\frac{\lambda d}{\pi\sigma_0}\right)^2} \quad (5)$$

To relate the beam waist in focus σ_0 as well as the parameter a to the magnification, 6 magnifications i.e. $12.5\times$, $15.0\times$, $17.5\times$, $20.0\times$, $22.5\times$, $25.0\times$, are configured to acquire the images of the same sphere. The magnifications are obtained through zooming. The magnification of $12.5\times$ approximately corresponds to the minimum magnification that renders the sphere visible in our experiment, while

$25.0\times$ approximates to the maximum magnification that confirms that a full revolution of the sphere remains in the field of view (FOV). The PSF of each magnification is modelled by creating an optimization problem and solving it with least square curve fitting. The overall fitting error of the 6 experimental PSFs is 5.00%. The experimental PSFs acquired from images with magnification of $12.5\times$ and $25.0\times$ are shown in Figure 3 (a) and (d) respectively. The color of the voxel indicates the intensity of PSF response. (b) and (e) represent the modelled PSFs of the two magnifications. Voxels in 3D space are converted to a 1D space with horizontal axis approximating the optical axis and vertical axis displaying the intensity. The 3D voxels on the slice in (a) and (b) match the 1D points in the box in (c) according to the same color. The experimental PSF differentiation between two magnifications is evident in (a) and (d). By transforming the 3D space to 1D functional, we can intuitively visualize the distribution of the experimental PSF (blue dots) and the modelled PSF (red dots), as well as showing the differences between them.

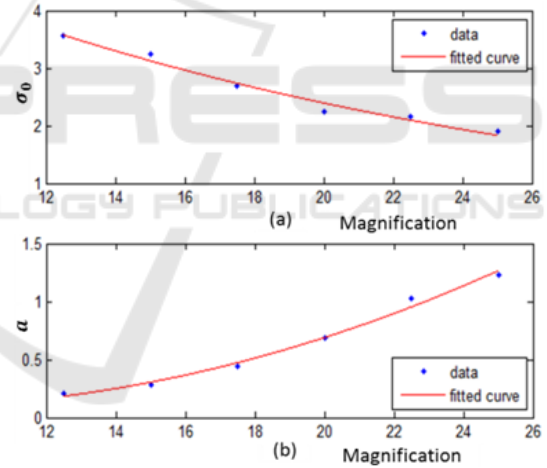


Figure 4: Fitting of σ_0 and the parameter a estimated from 6 magnifications. σ_0 is fitted by exponential function as shown in (a) while a is fitted by quadratic function in (b).

The parameters for our modelling ρ_1 , ρ_2 and ρ_3 have proved to be constant regardless of magnifications: $\rho_1 = 0.0041$, $\rho_2 = 1.0549$ and $\rho_3 = 2.9 \times 10^{-5}$. The beam waist σ_0 and parameter a relevant to the 6 magnifications are estimated as depicted in Figure 4. To minimize the fitting error on the observed data, the parameters are fitted as an exponential and a quadratic function respectively by using Eq. (6) and Eq. (7), with x representing magnification and p_1 to p_5 being the parameters.

$$\sigma_0 = p_1 \cdot e^{p_2 x} \quad (6)$$

$$a = p_3 x^2 + p_4 x + p_5 \quad (7)$$

The PSF of any 3D image between $-\infty$ and $+\infty$ along optical axis can be modelled as depicted in section 2.3. The modeling is implemented with the focal plane set at the COR. However, in most imaging cases the focal plane is not in line with the COR. Consequently, the modelled PSF will be shifted along the optical axis by the same shift as the focal plane. Besides, the length of the PSF along optical axis is determined by the size of 3D image and the resolution r , because in FBP 3D reconstruction each voxel in the 3D image corresponds to each pixel in the 2D images. The NA is the effective value achieved from interpolation relating to the magnification. The relationship between effective NA and magnification can be found in the product manual of the Leica objective lens.

2.4 Deconvolution of 3D Images in Coronal Plane

The modelled PSF consists of multiple 2D Gaussian patterns along optical axis. Therefore, the 3D image can be deconvolved slice by slice along its depth axis that is parallel to the optical axis. As the slices are coronal sections, the deconvolution is implemented on the 3D image R in the coronal plane as follows:

$$D_{(x,y,d)} = R_{(x,y,d)} ** p_{(s,t,d)} \quad (8)$$

R is the reconstructed 3D image with the depth axis d parallel to the optical axis of the PSF. $**$ stands for the operation of deconvolution. Considering the shifted focal plane and the reconstruction symmetry, deconvolution of R' , the opposite view of R projected along d , is executed by applying Eq. (9).

$$D'_{(x,y,d)} = R'_{(x,y,d)} ** p_{(s,t,d)} \quad (9)$$

The transform from R to R' is conducted by a matrix rotation of 180° centered by the COR. The 3D image with the deconvolution is then achieved by combining D and 180° back rotation of D' .

3 EXPERIMENTS

3.1 Image Comparison of Deconvolution

With respect to the magnifications, the experiments were conducted on images at 2 different magnifications. One is a zebra finch embryo in

fluorescence mode with magnification $13.83 \times$ and focal plane shifted by $-0.93mm$. Considering the resolution limit and the 3D image size, the calculated defocus of the PSF along the optical axis ranges from $-6.303mm$ to $8.063mm$. The deconvolution is performed using Lucy-Richardson algorithm with 10 iterations. The result for the coronal slice is shown in Figure 5 (b) and for the horizontal slice in Figure 5 (d). The corresponding slices without deconvolution are displayed in Figure 5 (a) and (c). The comparisons of intensity profile along a line with (red) and without (blue) deconvolution are presented in (e) and (f) respectively. In Figure 6 another sample is depicted. This is a sample from a 3dpf batch of zebrafish larvae. The magnification and the shifted focal plane are separately $49.98 \times$ and $-0.5mm$, with the computed defocus of PSF as between $-2.242mm$ and $3.246mm$. Figure 6 (a) and (b) are the slices before deconvolution in two orthogonal planes, while (c) and (d) corresponds to the deconvolution results. By visually comparing (c) and (d) we conclude that the performance in horizontal plane is as good as it is in coronal plane. This means that deconvolution in the coronal plane simultaneously improves the quality of the image in the horizontal plane. From a comparison of the quantitative intensity profile for each colored line, we state that the proposed deconvolution sharpens and refines the 3D reconstructed images. It enhances the strong signals and makes the intensity profile more distinct.

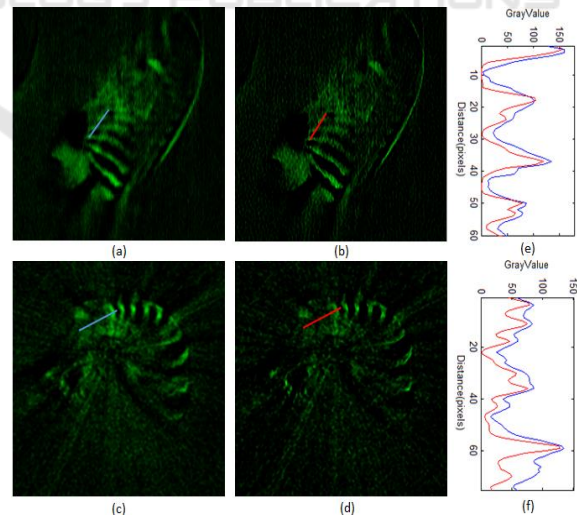


Figure 5: Deconvolution results. (a) The coronal slice of the 3D zebra finch with obvious blur around the ribs. (b) Distinct texture appears around the ribs after the deconvolution. (e) The comparison of intensity profiles along a line in (a) and (b). (c) and (d) The horizontal slice comparisons with the line intensity profiles shown in (f).

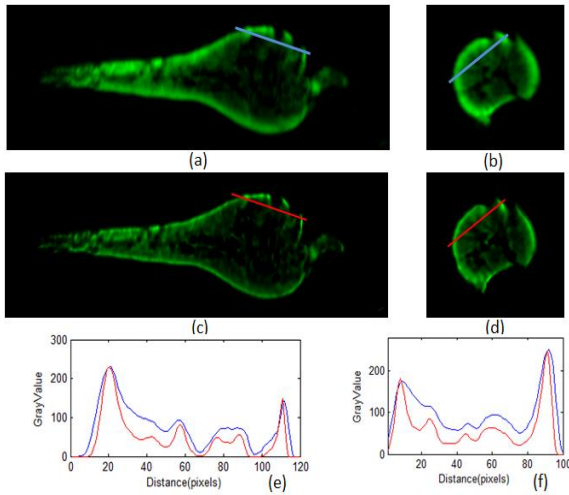


Figure 6: Coronal and horizontal slices of 3D zebrafish before ((a) and (b)) and after ((c) and (d)) deconvolution. The deconvolution highlights the strong signals and makes the texture more visible. The figure below (a) and (c) compares the intensity profile of the same line before (labelled as blue) and after (labelled as red) deconvolution, so does the figure below (b) and (d).

3.2 Image Blur Measurement on Slices

To quantify the image blur of each slice, 3 metrics from literatures, i.e. the just noticeable blur (JNB) measure (Ferzli et al., 2009), the cumulative probability of blur detection (CPBD) measure (Narvekar et al., 2009) and the frequency measure (FM) (De et al., 2013) are employed to evaluate the performance. Both the JNB and CPBD measure acquire sharpness metric by detecting and quantifying the blur in the spatial domain. Different from JNB and CPBD, the FM measure quantifies the sharpness in the frequency domain with an easier and more efficient approach. All the three metrics characterize the sharpness of an image, so the measure increases at improved image quality.

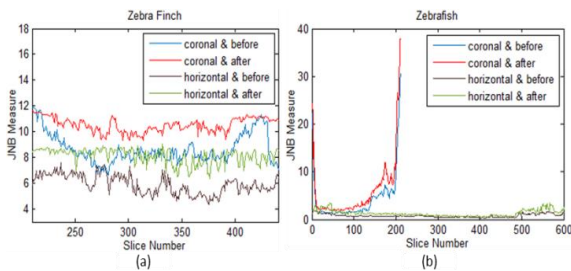


Figure 7: (a) JNB measure on the zebra finch data with magnification 13.83 ×. (b) JNB Measure on the zebrafish data with magnification 49.98 ×. Coronal and horizontal are the two orthogonal planes displaying the 3D image.

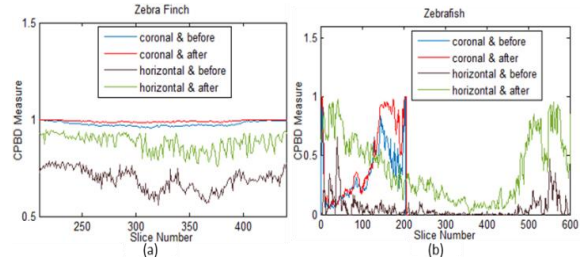


Figure 8: (a) CPBD measure on the zebra finch with magnification 13.83 ×. (b) CPBD Measure on the zebrafish with magnification 49.98 ×.

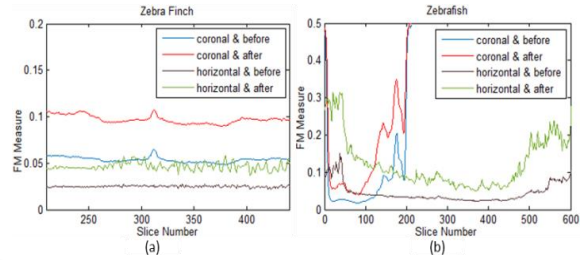


Figure 9: The FM before and after deconvolution on the two 3D image data. (a) FM measure on the zebra finch with magnification 13.83 ×. (b) FM Measure on the zebrafish with magnification 49.98 ×.

While experiments in section 3.1 give us a qualitative comparison between the deconvolved slice and non-deconvolved slice, in this section we quantitatively look into all the slices in different orthogonal planes with the three image sharpness measurements (i.e. JNB, CPBD and FM). From Figure 7 to Figure 9 we can see that, no matter what measure is used, the deconvolved slices in both planes have higher measurement values compared with the image slices without deconvolution. This means that on all slices, the deconvolution deblurs the images and significantly improves the image quality.

3.3 Quantitative 3D Image Quality Improvement of Deblur

To further quantify the deblur of the deconvolution results on the original reconstructed 3D data across the planes, we present the 3D image quality improvement criterion of deblur as I_{3d} in Eq. (10). Improvement in three orthogonal individuals are combined and encoded as a whole and each of them are represented as Eq. (11) to Eq. (13).

Table 1: 3D image quality improvement of 10 zebrafish embryos based on JNB Measure.

	01	02	03	04	05	06	07	08	09	10
\mathcal{G}	0.16	0.21	0.15	0.21	0.29	0.24	0.22	0.16	0.20	0.25
PSF_m	1.35	2.10	1.41	3.23	1.54	1.50	1.50	1.37	1.45	1.70

* \mathcal{G} -- Gaussian-based blind deconvolution. PSF_m -- PSF based modelling deconvolution. 10 zebrafish embryos correspond to 01-10 with age ranging from 3dfp to 7dfp. Magnification for 01-05 is $24.98 \times$ while for 06-10 is $22.45 \times$.

Table 2: 3D image quality improvement of 6 zebrafish brain based on JNB Measure.

	01	02	03	04	05	06
\mathcal{G}	0.25	0.29	0.26	0.24	0.01	0.21
PSF_m	0.41	0.49	2.55	0.17	1.15	1.20

* 6 zebrafish embryo brains correspond to 01-06 with age ranging from 6dfp to 7dfp. Magnification for 01-02 is $20.98 \times$ while for 03-06 is $15.98 \times$.

Table 3: 3D image quality improvement of 7 chicken heart based on JNB Measure.

	01	02	03	04	05	06	07
\mathcal{G}	0.24	0.16	0.19	0.26	0.27	0.18	0.32
PSF_m	0.93	0.49	0.29	1.15	0.49	0.38	1.07

* 7 chicken embryo hearts at different stages correspond to 01-07. Magnification for 01 is $15.00 \times$, while for 03-06 is $11.75 \times$ and 07 is $10.00 \times$.

$$I_{3d} = \sqrt{\left(\frac{1}{N_x} \sum_{ix=1}^{N_x} I_{ix}\right)^2 + \left(\frac{1}{N_y} \sum_{iy=1}^{N_y} I_{iy}\right)^2 + \dots + \left(\frac{1}{N_z} \sum_{iz=1}^{N_z} I_{iz}\right)^2} \quad (10)$$

$$I_{ix} = \frac{M_{ix}^d - M_{ix}^r}{M_{ix}^r} \quad (11)$$

$$I_{iy} = \frac{M_{iy}^d - M_{iy}^r}{M_{iy}^r} \quad (12)$$

$$I_{iz} = \frac{M_{iz}^d - M_{iz}^r}{M_{iz}^r} \quad (13)$$

Where M_{ix}^d and M_{ix}^r are the i th deconvolved and original reconstructed slice in x plane respectively. By employing the image quality improvement of deblur I_{3d} , deconvolution performance of two different methods on the same data turns to be comparable.

We here applies our deconvolution method to 23 more 3D data, which contains 3 categories of samples i.e. zebrafish embryo, zebrafish embryo brain and

chicken embryo heart. They are in different stages and are acquired at different magnifications. It is important to know that all the measurements in this paper cannot assess the image blur across different data, but it provides us with a comparative evaluation of image deblur on the same data. Taking advantage of this, we compare the presented deconvolution method with the most commonly used Gaussian-based blind deconvolution (Chan *et al.*, (1998)). The Gaussian kernel size is set to 7 for all slices. As the most robust measurement among CPBD, JNB and FM, JNB is employed to evaluate the image blur of each slice. The results of the 3 categories of samples are presented in Table 1 to Table 3. For all the 23 data, our deconvolution approach outperforms the Gaussian-based deconvolution, thereby indicating the success of the method.

4 CONCLUSIONS

In this paper we have focused on 3D image deblur and quality improvement, under the condition of the limitation of small NA for imaging of large samples. We investigated and modeled the PSF along the optical axis, exploring the influence of magnification on PSF. The sample of a single GFP sphere is prepared with the protocol in section 2.2. The experimental PSF is then modelled to deconvolve the 3D image in a coronal plane. A number of measures for image blur are employed to convincingly evaluate the performance of the deconvolution. They provide quantitative information about how much improvement is achieved. The overall improvement I_{3d} gives us a criterion to compare image quality improvement regardless of different data. All the experimental results including the image comparisons and quantitative measures sustain the effectiveness of the proposed PSF modelling and deconvolution methodology.

The deconvolution results presented in this paper represent a proof of concept. The datasets used in the experiments are composed of 25 samples (i.e. 4 categories: zebrafish embryo, zebra finch embryo, zebrafish brain and chicken heart). Regarding the evaluation of performance on a large scale of dataset, our data are far from perfect in terms of 'large dataset'. However, it presents a clear idea that our model is not constrained by several samples, it also works on many other types of objects or images. This will help to explain its potential capability of improving image quality on more 3D data, including those from other OPT imaging systems, which is a part of our current work. In the future we will take

more effort on further generalizing the model to other imaging set-ups. In addition, the fluorescent sphere used in the experiments is fix-sized. The effect of sphere size on PSF modelling and deblur performance will be investigated afterwards.

REFERENCES

- Sharpe, J. *et al.*, 2002. Optical projection tomography as a tool for 3D microscopy and gene expression studies. *Science* (80-.), vol. 296, no. 5567, pp. 541–545, 2002.
- Walls, J. R., Sled, J. G., Sharpe, J. and Henkelman, R. M., 2007. Resolution improvement in emission optical projection tomography. *Phys. Med. Biol.*, vol. 52, no. 10, p. 2775.
- McNally, J. G., Karpova, T., Cooper, J. and Conchello, J. A., 1999. Three-dimensional imaging by deconvolution microscopy. *Methods*, vol. 19, no. 3, pp. 373–385.
- Kak, A. C. and Slaney, M., 2001. Principles of computerized tomographic imaging. *SIAM*.
- Chen, L. *et al.*, 2012. Incorporation of an experimentally determined MTF for spatial frequency filtering and deconvolution during optical projection tomography reconstruction. *Opt. Express*.
- Chen, L., Andrews, N., Kumar, S., Frankel, P., McGinty, J. and French, P. M. W., 2013. Simultaneous angular multiplexing optical projection tomography at shifted focal planes. *Opt. Lett.*, vol. 38, no. 6.
- Miao, Q., Hayenga, J., Meyer, M. G., Neumann, T., Nelson, A. C. and Seibel, E. J., 2010. Resolution improvement in optical projection tomography by the focal scanning method. *Opt. Lett.*, vol. 35, no. 20, pp. 3363–5.
- Xia, W., Lewitt, R. M. and Edholm, P. R., 1995. Fourier correction for spatially variant collimator blurring in SPECT. *IEEE Trans. Med. Imaging*, vol. 14, no. 1, pp. 100–115.
- Darrell, H. Meyer, K. Marias, M. Brady, and J. Ripoll., 2008. Weighted filtered backprojection for quantitative fluorescence optical projection tomography. *Phys. Med. Biol.*, vol. 53, no. 14, pp. 3863–81.
- McErlean, C. M., Bräuer-Krisch, E., Adamovics, J. and Doran, S. J., 2016. Assessment of optical CT as a future QA tool for synchrotron x-ray microbeam therapy. *Phys. Med. Biol.*, vol. 61, no. 1, pp. 320–37.
- van der Horst, J., and Kalkman, J., 2016. Image resolution and deconvolution in optical tomography. *Opt. Express*, vol. 24, no. 21, pp. 24460–24472.
- Tang, X., van der Zwaan, D., Zammit, M., Rietveld, A., K. F. D. and Verbeek, F. J., 2017. Fast Post-Processing Pipeline for Optical Projection Tomography. *IEEE Trans. Nanobioscience*, vol. 16, no. 5, pp. 367–374, Jul.
- Kogelnik, H. and Li, T., 1966. Laser Beams and Resonators. *Proc. IEEE*, vol. 54, no. 10, pp. 1312–1329.
- Ferzli, R. and Karam, L. J., 2009. A no-reference objective image sharpness metric based on the notion of Just Noticeable Blur (JNB). *IEEE Trans. Image Process.*, vol. 18, no. 4, pp. 717–728.
- Narvekar, N. D. and Jaram, L. J., 2009. An improved no-reference sharpness metric based on the probability of blur detection. *IEEE Int. Work. Qual. Multimed. Exp.*, vol. 20, no. 1, pp. 1–5.
- De, K. and Masilamani, V., 2013. Image Sharpness Measure for Blurred Images in Frequency Domain. *Procedia Eng.*, vol. 64, no. Complete, pp. 149–158.
- Chan, T.F. and Wong, C.K., 1998. Total variation blind deconvolution. *IEEE Transactions on Image Processing*, vol. 7, no. 3, pp. 370–375.